JOURNAL OF SPACECRAFT AND ROCKETS
Vol. 35, No. 4, July–August 1998

Three-Dimensional Modeling, Estimation, and Fault Diagnosis of Spacecraft Air Contaminants

Anand P. Narayan* and W. Fred Ramirez†
University of Colorado, Boulder, Colorado 80309-0424

A description is given of the design and implementation of a method to track the presence of air contaminants aboard a spacecraft using an accurate physical model and of a procedure that would raise alarms when certain tolerance levels are exceeded. Because our objective is to monitor the contaminants in real time, we make use of a state estimation procedure that filters measurements from a sensor system and arrives at an optimal estimate of the state of the system. The model essentially consists of a convection–diffusion equation in three dimensions, solved implicitly using the principle of operator splitting, and uses a flowfield obtained by the solution of the Navier–Stokes equations for the cabin geometry, assuming steady-state conditions. A novel implicit Kalman filter has been used for fault detection, a procedure that is an efficient way to track the state of the system and that uses the sparse nature of the state transition matrices.

Nomenclature

$\boldsymbol{A}_1$	= state transition matrix (left-hand side)
$\boldsymbol{A}_2$	= state transition matrix (right-hand side)
c_u, c_1, c_2	= empirical constants used in the k–ϵ turbulence model
D_M	= mass diffusivity, $m^2\ s^{-1}$
$\boldsymbol{f}$	= contaminant source term, kg $m^{-3}\ s^{-1}$
$\boldsymbol{H}$	= measurement matrix
$\boldsymbol{L}_m$	= implicit Kalman gain
l	= loss function
$\boldsymbol{Q}$	= covariance matrix of the model noise
$\boldsymbol{Q}_m$	= concentration vector
q	= concentration of contaminant, kg m^{-3} (vol%)
$\boldsymbol{q}$	= discrete analog of contaminant concentration, kg m^{-3} or vol%
$\boldsymbol{R}$	= covariance matrix of the measurement noise
$\boldsymbol{r}$	= row unity matrix
t	= time, s
$\boldsymbol{u}$	= velocity vector
u, v, w	= velocity components in the coordinate directions, $m\ s^{-1}$
$\boldsymbol{x}(k)$	= state vector
$\hat{\boldsymbol{x}}$	= estimate of state
$\tilde{\boldsymbol{x}}$	= estimation error
x, y, z	= coordinate directions
$z(i)$	= measurement signal
$\boldsymbol{\alpha}, \boldsymbol{\beta}$	= zero-mean white Gaussian processes
λ	= second viscosity coefficient
μ	= molecular viscosity coefficient
ρ	= density of fluid, kg m^{-3}
$\sigma_k, \sigma_\epsilon$	= empirical constants used in the turbulence model
$\boldsymbol{\Phi}_k$	= error functional

Subscripts

n, p, r	= mesh indices in the coordinate directions

Superscripts

D	= down
E	= east
N	= north
S	= south
U	= up
W	= west

Received Aug. 18, 1997; revision received Jan. 23, 1998; accepted for publication Jan. 26, 1998.

*Graduate Student, Department of Chemical Engineering.
†Professor, Department of Chemical Engineering.

Introduction

INDOOR pollution has been the subject of considerable research. Indoor pollution becomes an extremely critical factor in long-term flight missions, such as the Mars mission or in the space station. Indoor air quality is also an issue related to energy conservation in buildings and the thermal comfort and health of building occupants. This work mainly pertains to the detection and simulation of air contaminants in the space station, though much of the work is easily extended to buildings and issues of ventilation systems. Control of air contaminants is a crucial factor in the safety considerations of crewed space flight. We propose a method to track the presence of contaminants using an accurate physical model and also develop a robust procedure that would raise alarms when certain tolerance levels are exceeded. This paper discusses the modeling of airflow inside a spacecraft and the consequent dispersal pattern of contaminants. Because our objective was also to monitor the contaminants online, we developed a state estimation procedure that makes use of the measurements from a sensor system and arrives at an optimal estimate of the contamination in the system as a function of time and space.

Most of this work was undertaken under the auspices of NASA's Advanced Environmental Monitoring and Control Program, with a view to develop an intelligent monitoring system for space station missions. Also of specific relevance are the crewed missions to Mars, the Mars Short Visit, the Mars Human-Tended Outpost, and the Mars Permanent Outpost, where astronauts are expected to spend between 7 and 600 days and where the luxury of returning to Earth for a cleanup in the case of a contaminant leak does not exist. Contaminants that are to be monitored include carbon dioxide, carbon monoxide, and volatile organics. According to NASA, primary chemicals of concern are nitrogen tetroxide, monomethyl hydrazine, ammonia, and halon 1301. There is an extensive body of literature in the area of environmental control aboard spacecraft.[1] The National Research Council has prescribed spacecraft maximum allowable concentrations (SMAC), which are not to be exceeded under any circumstances. These concentrations are based on studies that link contaminant concentrations to the impairment of normal human activities. Separately, scientists working in the Russian space program published their own maximum allowable concentrations, and current research in the area is focusing on blending the two because there are substantial differences in the limits, with the U.S. limits being in general more relaxed. Researchers at the Jet Propulsion Laboratory and other laboratories are working on advanced sensors that will be able to detect smaller amounts of contaminant and that will have faster response times. Our work focuses on the design and implementation of control and fault diagnosis systems that use the sensor capabilities and that analyze the data to achieve the control objectives specified through the SMAC.

Modeling of Air Contaminant Dispersal

One of the goals of this work was the development of the full-blown three-dimensional transport model for the airborne contaminants. Previous work has either used the control-volume approach, in which the cabin was modeled as a collection of well-mixed reactors,[2] or used a space-averaged two-dimensional model.[3]

Assuming a constant density of spacecraft atmosphere and a constant molecular diffusivity, the differential mass balance of the airborne contaminant results in the following fundamental three-dimensional convection–diffusion transport model:

$$\frac{\partial q}{\partial t} + \boldsymbol{u} \cdot \boldsymbol{\nabla} q = D_M \boldsymbol{\nabla}^2 q + f \tag{1}$$

In this work, we are assuming that the contaminant is passive, i.e., it is transported with air at the same velocity in the field. In addition, we are assuming that the contaminant undergoes no chemical or physical transformations during its transport.

Equation (1) is applicable to both laminar and turbulent flow. However, in the case of turbulent flow, the velocity vector is extremely random, and so we resort to using the time-averaged equations instead. The idea is to average the Fickian model over a time interval long enough for the integral of the instantaneous fluctuations to become zero. For the case of turbulent flow, therefore, we treat both the flow velocity and the concentration as stochastic quantities. We will discuss the specifics of how we treat the turbulence in the section on airflow modeling. The equation, then, for the case of turbulent flow is

$$\frac{\partial \bar{q}}{\partial t} + \bar{\boldsymbol{u}} \cdot \boldsymbol{\nabla} \bar{q} = D_M \boldsymbol{\nabla}^2 \bar{q} + \bar{f} \tag{2}$$

where the overbar indicates time-averaged quantities.

We solve the model equation (1) using a simple finite differencing scheme. The diffusive terms are discretized using a second center difference scheme, whereas the convective terms are discretized using the upwind differencing scheme to eliminate oscillatory effects in the solution. The application of the center difference approximation of the time derivative yields the following discrete analog of the three-dimensional transport model:

$$\begin{aligned}
\frac{q^{m+1}_{n,p,r} - q^{m}_{n,p,r}}{\Delta t} = -\frac{1}{2}\Bigg(& u_{n,p,r} \frac{\left[q^{E}_{n,p,r}\right]^{m+1} - \left[q^{W}_{n,p,r}\right]^{m+1}}{\Delta x} \\
& + u_{n,p,r} \frac{\left[q^{E}_{n,p,r}\right]^{m} - \left[q^{W}_{n,p,r}\right]^{m}}{\Delta x} + v_{n,p,r} \frac{\left[q^{S}_{n,p,r}\right]^{m+1} - \left[q^{N}_{n,p,r}\right]^{m+1}}{\Delta y} \\
& + v_{n,p,r} \frac{\left[q^{S}_{n,p,r}\right]^{m} - \left[q^{N}_{n,p,r}\right]^{m}}{\Delta y} + w_{n,p,r} \frac{\left[q^{D}_{n,p,r}\right]^{m+1} - \left[q^{U}_{n,p,r}\right]^{m+1}}{\Delta z} \\
& + w_{n,p,r} \frac{\left[q^{D}_{n,p,r}\right]^{m} - \left[q^{U}_{n,p,r}\right]^{m}}{\Delta z} \Bigg) \\
& - \left[\mu_{n+1,p,r} \frac{q^{m+1}_{n+1,p,r} - q^{m+1}_{n,p,r}}{\Delta x^2} - \mu_{n,p,r} \frac{q^{m+1}_{n,p,r} - q^{m+1}_{n-1,p,r}}{\Delta x^2} \right. \\
& \left. + \mu_{n+1,p,r} \frac{q^{m}_{n+1,p,r} - q^{m}_{n,p,r}}{\Delta x^2} - \mu_{n,p,r} \frac{q^{m}_{n,p,r} - q^{m}_{n-1,p,r}}{\Delta x^2} \right] \\
& - \left[\mu_{n,p+1,r} \frac{q^{m+1}_{n,p+1,r} - q^{m+1}_{n,p,r}}{\Delta y^2} - \mu_{n,p,r} \frac{q^{m+1}_{n,p,r} - q^{m+1}_{n,p-1,r}}{\Delta y^2} \right. \\
& \left. + \mu_{n,p+1,r} \frac{q^{m}_{n,p+1,r} - q^{m}_{n,p,r}}{\Delta y^2} - \mu_{n,p,r} \frac{q^{m}_{n,p,r} - q^{m}_{n,p-1,r}}{\Delta y^2} \right] \\
& - \left[\mu_{n,p,r+1} \frac{q^{m+1}_{n,p,r+1} - q^{m+1}_{n,p,r}}{\Delta z^2} - \mu_{n,p,r} \frac{q^{m+1}_{n,p,r} - q^{m+1}_{n,p,r-1}}{\Delta z^2} \right. \\
& \left. + \mu_{n,p,r+1} \frac{q^{m}_{n,p,r+1} - q^{m}_{n,p,r}}{\Delta z^2} - \mu_{n,p,r} \frac{q^{m}_{n,p,r} - q^{m}_{n,p,r-1}}{\Delta z^2} \right] + f^{m+1}_{n,p,r}
\end{aligned} \tag{3}$$

where Δt is the time discretization step and the superscript $m = 0, 1, 2, \ldots$, is used to identify an instance $t = (m+1)\Delta t$ for which the solution of the equation is sought.

The like terms in Eq. (3) are collected to obtain the equation in matrix form for a single spatial mesh point (n, p, r):

$$\boldsymbol{A} \cdot \boldsymbol{q} = \boldsymbol{d}$$

The solution scheme used is the alternating direction implicit scheme, which invokes the property of operator splitting[4] and converts the problem into a system of three tridiagonal matrix equations, which can be solved using the Thomas algorithm.[5] The convective operators are discretized using an upwind first-order scheme, whereas the diffusive terms are discretized using a second-order center difference scheme. The time operator is a simple forward difference term. The truncation error is of $\mathcal{O}(\Delta x^2, \Delta y^2, \Delta z^2, \Delta t)$.

Modeling of Airflow Within an Enclosure

In the preceding section, we developed the contaminant dispersal model, which needed a wind field as an input. In this section, we develop a method to solve for the wind field in the cabin.

Airflows inside enclosures have been a subject of active interest within the building systems community. Computational fluid dynamics (CFD) has been used for predicting room air movement since the 1970s. There even exists public domain software described by Kurabuchi et al.,[6] called EXACT3, which is a three-dimensional finite difference computer program for simulating buoyant turbulent airflow within buildings. In recent years, much effort has been made to enhance CFD as a reliable tool for the evaluation of airflows. Most of the work has remained computational, though a few validating experimental results also exist in the literature. The International Energy Agency, though a subsidiary research group Annex 20, measured velocities, temperatures, and turbulence velocity scales in full-scale rooms.[7] Canadian researchers[8] did studies on the correlation between the velocity of the inlet jet and the floor velocity and proposed a jet momentum number that would measure the energy contained in the diffuser jet relative to the room air volume.[9] In this paper, we use CFD to provide the information regarding the flow, which is then used as an input to the mathematical model for the diffusion and for the procedure that estimates the current concentration of contaminants in the cabin. This development marks an important step in our estimation procedure inasmuch as the accuracy of the procedure is largely dependent on the accuracy of the flow model because most of the transport is occurring through convective diffusion.

A detailed knowledge of the flowfield is required to ensure that the ventilation system is performing adequately and to provide information about local variations in the concentration profile of the contaminants. Another advantage in using CFD is that it enables us to calculate quantities such as turbulence intensity, which have direct effects on the comfort level of people inside the cabin. Research has shown that lower turbulence intensities contribute to higher comfort levels.[10]

We assume that the airflow is steady and solve the three-dimensional Navier–Stokes equations for the appropriate boundary and initial conditions. Earlier work by Skliar and Ramirez[3] used a two-dimensional flowfield as an input to the state estimation procedure. In a significant development in this work, we consider modeling the three-dimensional geometry of the space station module of Son and Barker.[11] The two-dimensional case has the advantage of requiring far less computational time, whereas it suffers from a lack of information about the third dimension.

Airflows inside enclosures are usually turbulent, random, and highly recirculating.[10] In this work, we solve the equations for both laminar and turbulent cases. The geometry chosen here (Fig. 1) and that used by Son and Barker[11] accurately represent the U.S. Lab-A module in the International Space Station.

We used this geometry for our simulations inasmuch as the station is the domain for which this research is being done and to have an experimental set of results to validate our simulations. The simulated cabin is 6 m long, 2 m wide, and 2 m high (approximately $20 \times 7 \times 7$ ft). There are two inlets and two outlets for the air supply. The temperature and humidity control (THC) is the primary air supply, which supplies regulated air into the cabin and is one of the

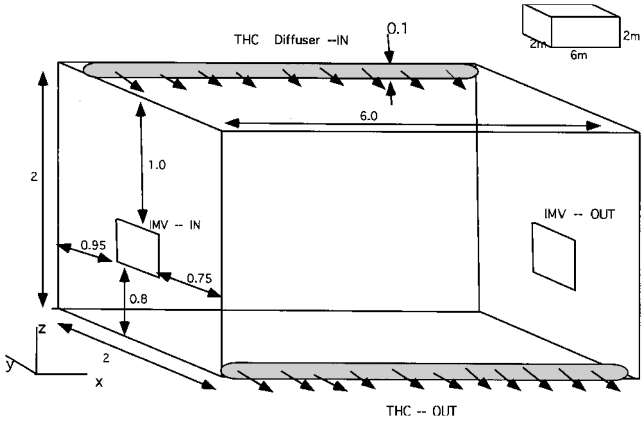

Fig. 1 Model cabin.

primary subsystems in the environmental control and life support systems for the space station.[11] The intermodule ventilation (IMV) airflow assemblies are used to interchange airflow between modules. One would expect that the THC air is relatively contaminant free because it is filtered, whereas the IMV could have trace contaminants generated in other modules, both routine contaminants and those released due to accidents.

The airflow model is based on the continuity equation, the Navier–Stokes equation, the thermal energy equation, and the concentration equation together with the k–ϵ turbulence model equations, for the case of turbulent flow. The k–ϵ model uses the kinetic energy of turbulence k and its dissipation rate ϵ to model the turbulence. This introduces two additional transport equations. In the k–ϵ model, the turbulent viscosity μ_t, also known as the eddy viscosity, is defined by the relation

$$\mu_t = \frac{C_\mu \rho k^2}{\epsilon} \tag{4}$$

For a rectangular cabin geometry, the equations of continuity and momentum for an incompressible flow are as follows.

Continuity:

$$\frac{\partial u}{\partial x} + \frac{\partial v}{\partial y} + \frac{\partial w}{\partial z} = 0 \tag{5}$$

Momentum:

$$\frac{\partial(\rho u)}{\partial t} + \frac{\partial(\rho u^2)}{\partial x} + \frac{\partial(\rho uv)}{\partial y} + \frac{\partial(\rho uw)}{\partial z}$$
$$= -\frac{\partial p}{\partial x} + \frac{\partial}{\partial x}\left(\lambda \nabla \cdot \boldsymbol{u} + 2\mu \frac{\partial u}{\partial x}\right) + \frac{\partial}{\partial y}\left[\mu\left(\frac{\partial v}{\partial x} + \frac{\partial u}{\partial y}\right)\right]$$
$$+ \frac{\partial}{\partial z}\left[\mu\left(\frac{\partial u}{\partial z} + \frac{\partial w}{\partial x}\right)\right] + \rho f_x \tag{6}$$

$$\frac{\partial(\rho v)}{\partial t} + \frac{\partial(\rho uv)}{\partial x} + \frac{\partial(\rho v^2)}{\partial y} + \frac{\partial(\rho vw)}{\partial z}$$
$$= -\frac{\partial p}{\partial y} + \frac{\partial}{\partial x}\left[\mu\left(\frac{\partial v}{\partial z} + \frac{\partial u}{\partial y}\right)\right] + \frac{\partial}{\partial y}\left(\lambda \nabla \cdot \boldsymbol{u} + 2\mu \frac{\partial v}{\partial y}\right)$$
$$+ \frac{\partial}{\partial z}\left[\mu\left(\frac{\partial w}{\partial y} + \frac{\partial v}{\partial z}\right)\right] + \rho f_y \tag{7}$$

$$\frac{\partial(\rho w)}{\partial t} + \frac{\partial(\rho uw)}{\partial x} + \frac{\partial(\rho vw)}{\partial y} + \frac{\partial(\rho w^2)}{\partial z}$$
$$= -\frac{\partial p}{\partial z} + \frac{\partial}{\partial x}\left[\mu\left(\frac{\partial u}{\partial z} + \frac{\partial w}{\partial x}\right)\right] + \frac{\partial}{\partial y}\left[\mu\left(\frac{\partial w}{\partial y} + \frac{\partial v}{\partial z}\right)\right]$$
$$+ \frac{\partial}{\partial z}\left(\lambda \nabla \cdot \boldsymbol{u} + 2\mu \frac{\partial w}{\partial z}\right) + \rho f_z \tag{8}$$

The equations were solved in a coupled manner using the fluid dynamics analysis package (FIDAP).[12] A finite element mesh grid was developed for the two-dimensional and the three-dimensional problems with specified nodal boundary conditions. An eight-node brick was used as the basic finite element for the purpose of discretization. The velocity components were approximated using trilinear interpolation functions within the elements. The pressure was discretized in a piecewise continuous manner, with the pressure degree of freedom associated with the element centroid. A segregated solver was used to solve the resulting nonlinear equations. The segregated solver decouples the equations for the purpose of solution and sequentially solves them, using the results of one equation in the next and so on. This increases the CPU time needed but conserves memory and has been found to be very useful for large mesh sizes. A variety of boundary conditions were tried, though for the sake of conciseness, only two cases will be discussed here. The convergence criterion was that the residuals of the computed quantities (velocity components and the pressure) be below 10^{-4}. Most of the computations were performed on the SGI Power Challenge Array, in a parallel mode with either two or three processors, available to us through the National Center for Supercomputing Applications, University of Illinois at Urbana–Champaign. The runs required varying times to converge, approximately in the range of 60 CPU hours for each.

Case 1: Laminar Flow

The geometry has already been described. For this case, we used an IMV flow rate of 0.15 m^3/s and a THC flow rate of 0.3 m^3/s. It is assumed that the outlet velocities remain constant throughout the ducts, which is ensured using an arrangement of vanes in the diffusers. The cabin is assumed to be isothermal. The ducts leading to the outlet are modeled using free boundary conditions, i.e., the values of the velocities are allowed to float to satisfy the Navier–Stokes equations. The no-slip boundary condition was invoked at all of the walls. We assume that the flow is laminar and that it is a steady flowfield.

Figures 2–4 show the flow profiles that we obtained. The contours of the magnitude of the velocities are shown as three slices of the cabin, one each near the top and bottom and one in the middle of the cabin to illustrate the variations. The slice near the bottom is mainly dominated by the exit through the THC duct. Note that the flow leaves at an angle to the duct due to the blast of air that blows in the x direction. The slice near the center clearly shows a velocity profile near the inlet and outlet of the IMV ducts. The flow spreads out throughout the room. The laminar case shows no recirculation cells. The slice from the top of the cabin shows the flow entering the cabin, and recirculation cells form as the jet curves downward.

Case 2: Turbulent Flow

Turbulence, in a sense, is still an unsolved problem. The presence of a length and a timescale much smaller than the physical problem presents a scenario where the exact solution to Eqs. (5–9) cannot be obtained. A statistical approach is usually used, and the equations are averaged over a timescale that is long compared to that of turbulent motion. The resulting averaged equations then describe the distribution of the mean velocity, pressure, temperature, and other quantities of interest. Detailed derivations of the equations can be found in any advanced book on fluid motion.[13] We use the two-equation model, briefly mentioned earlier. For isothermal flow with no mass transfer, the recommended set of model parameters was used:

$$c_u = 0.09, \qquad \sigma_k = 1.00, \qquad \sigma_\epsilon = 1.30$$
$$c_1 = 1.44, \qquad c_2 = 1.92 \tag{9}$$

Figures 5–7 are graphical representations of the turbulent flow simulations. Figure 5 shows the flow profile at the bottom slice. Unlike the laminar case, the flow dissipates quite rapidly, and the profile is composed of numerous recirculation cells. Figure 6 shows the center profile and the effects of the IMV flow. The contours here show the main blast of air coming through the duct and the two main

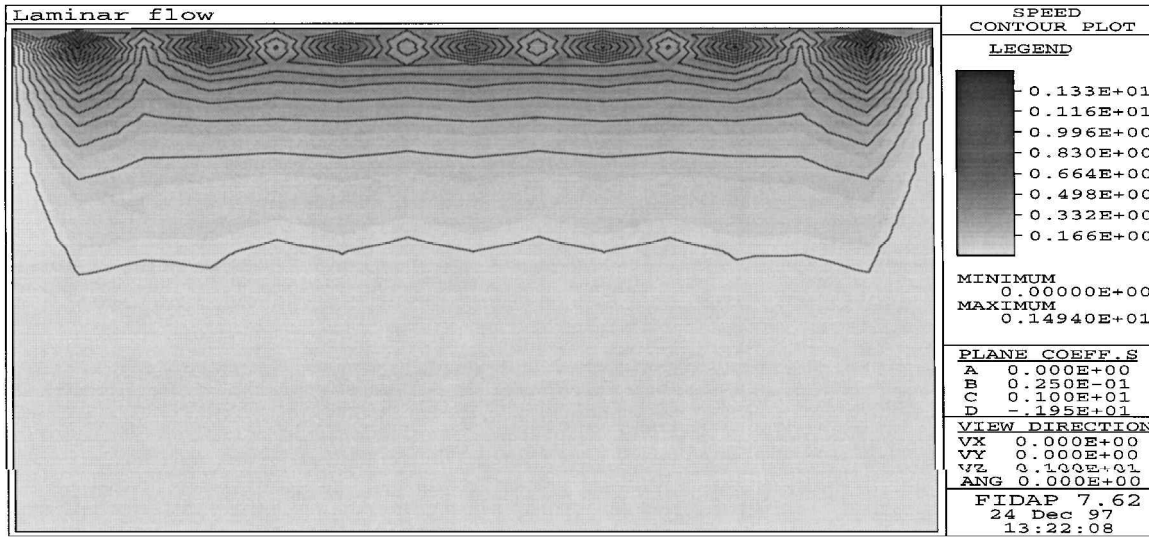

Fig. 2 Speed contour for the top slice (1.95 m), laminar flow.

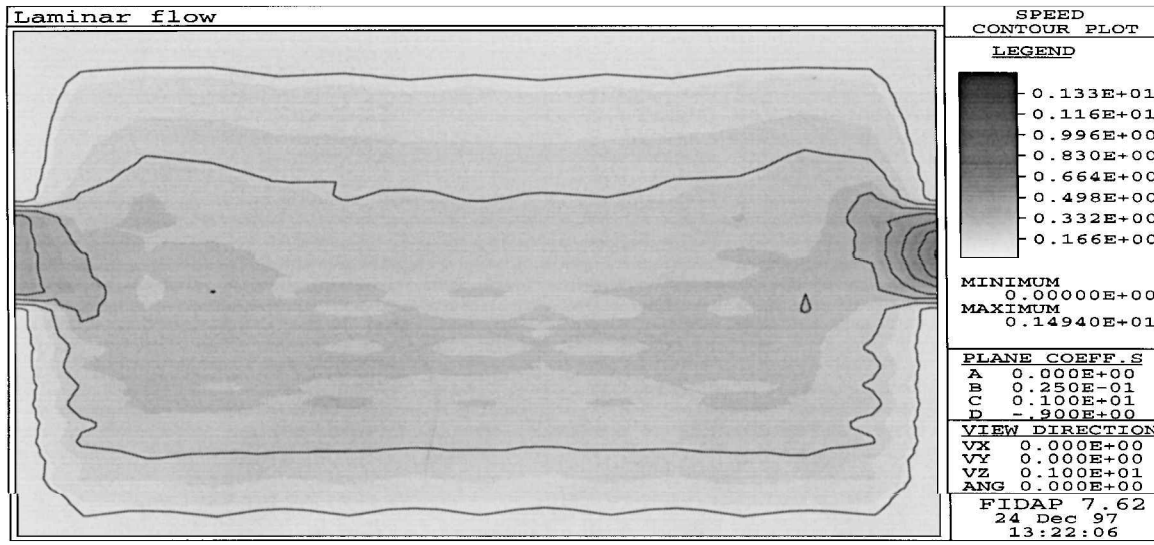

Fig. 3 Speed contour for the middle slice (0.9 m), laminar flow.

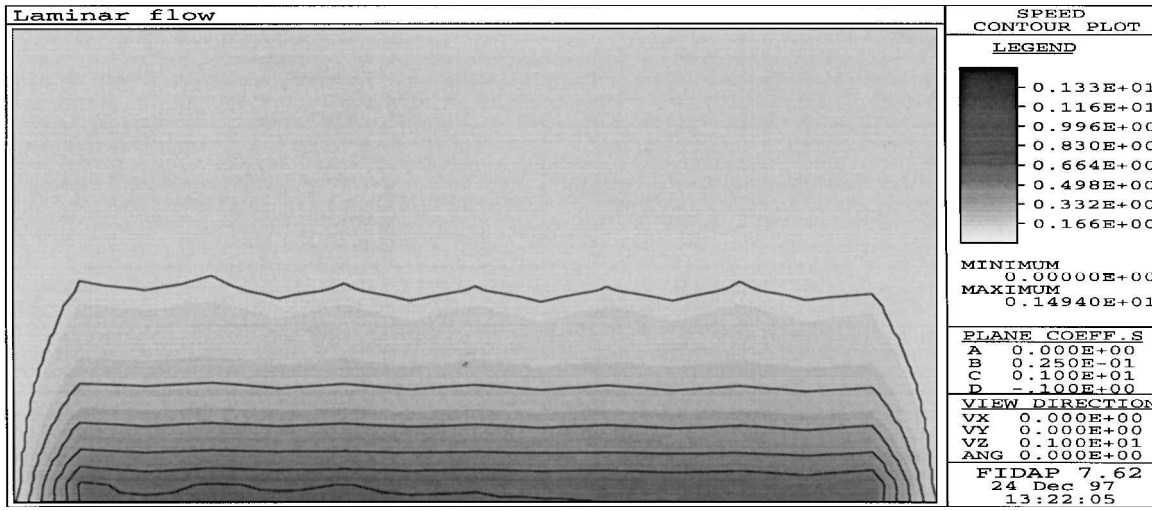

Fig. 4 Speed contour for the bottom slice (0.05 m), laminar flow.

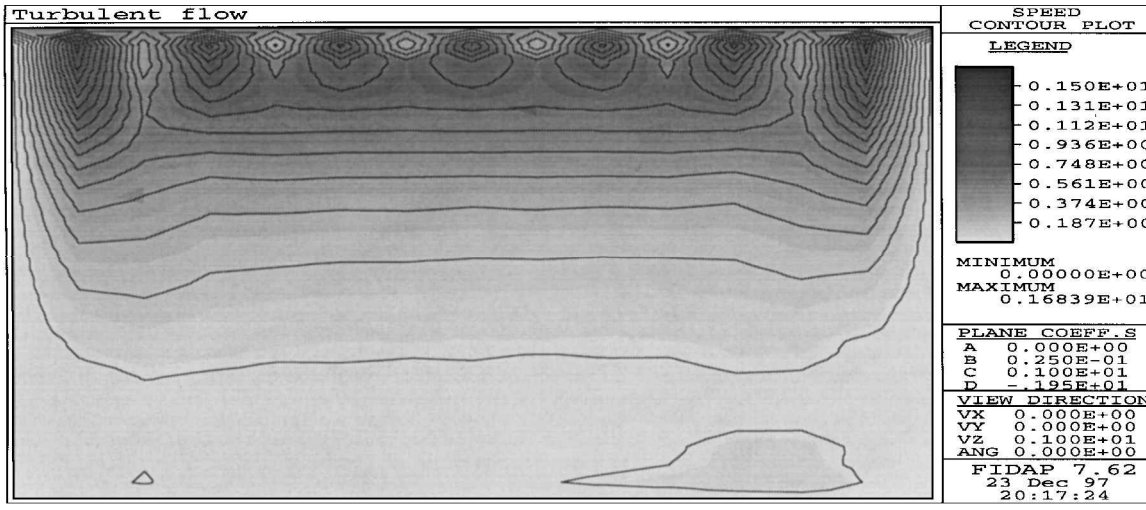

Fig. 5 Speed contour for the top slice (1.95 m), turbulent flow.

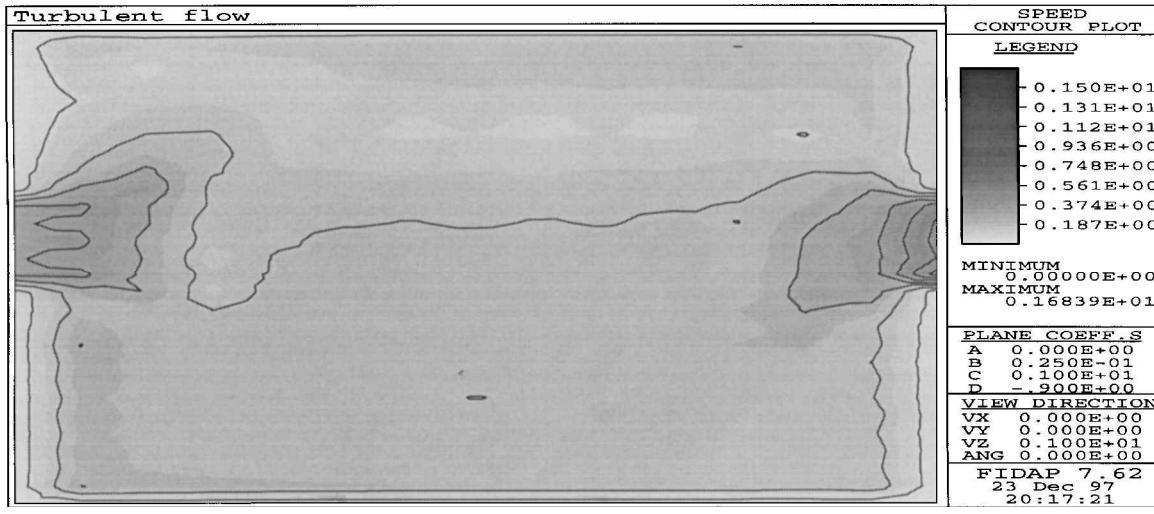

Fig. 6 Speed contour for the middle slice (0.9 m), turbulent flow.

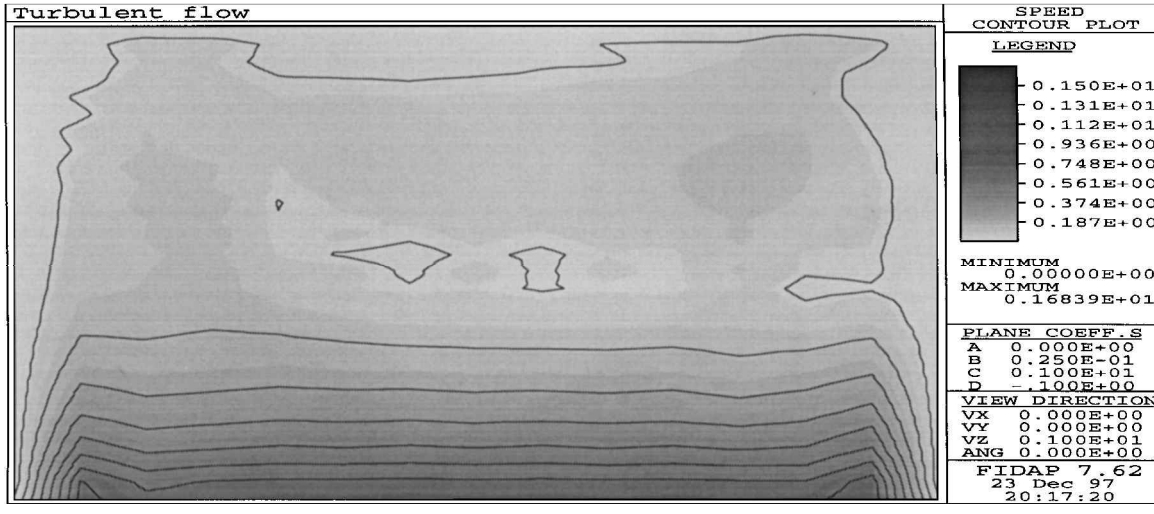

Fig. 7 Speed contour for the bottom slice (0.05 m), turbulent flow.

recirculation cells around the central duct. Figure 7 shows the top slice with the incoming jet of THC flow. The flow curves downward, separating from the ceiling in what is known as the Coanda effect.[10]

The turbulent flow profiles closely resemble those obtained experimentally by Son and Barker[11] in their space station chamber. The differences can be attributed to the minor differences in the geometry in the region of the hatches connecting the modules and the roundedness of their shuttle. The existence of recirculation cells is the significant difference between the laminar and the turbulent profiles. We believe that the actual flow in the space station will be mostly turbulent and that the profiles we obtain are characteristic of low-velocity turbulence flows.

Contaminant Dispersal Solution

We now proceed to test the working of our model by simulating some test cases. In this section, we use the wind field that we obtained in the sample cases to observe how contaminant dispersal occurs. We consider two separate cases, both of which represent actual space station contaminant scenarios.

Case 1: Steady-State Contamination

This case attempts to mimic the routine operation of the space station module. For this specific case, we are assuming a release of 20 mg of carbon dioxide over the first two time steps (of 4.5 s each). In addition, we have a steady input of carbon dioxide in the inlet streams. The cabin has a residual carbon dioxide concentration of 0.3 vol% for its initial condition. The THC air comes at a concentration of 0.5 vol% and the IMV with a concentration of 0.71 vol%. This would be realistic because the THC is filtered, and we could assume that one of the other modules has a lot of astronaut activity and, thus, the high carbon dioxide level. The simulation was done for about 300 time steps (about 1350 s). By this time, we observe a steady-state concentration distribution. Figure 8 shows the contamination levels at four different slices in the cabin, at levels 0.067, 0.67, 1, and 1.87 m from the floor of the cabin after about 1300 s. The surface plots of the slices closer to the middle of the room show similar profiles, and the exits and the consequent drop in concentration levels of the contaminant are clearly visible. This is due to the strong blast (relative to the rest of the cabin) of wind removing the contaminant through convective transport.

Case 2: Sudden Release of Carbon Dioxide

This would represent the case where carbon dioxide was used to extinguish a fire. A large release of carbon dioxide then would occur over a small time frame, and we wish to monitor how the contaminant levels fall off gradually. Figures 9 and 10 show the concentration levels 90 and 1500 s after the release. The surface plots and contours are shown at planar slices 0.067, 0.67, 1, and 1.87 m from the floor of the cabin. During these 1500 s, more than 70% of the released carbon dioxide has been flushed out from the room. Figure 9 shows the profiles 90 s after the release, which happened near the bottom-left-hand corner of the cabin (0.27, 0.14, and 0.17 m). In this figure, substantial amounts of the carbon dioxide are still present near the location of the occurrence, though the levels are dropping off near the outlets. In Fig. 10, which shows the profiles 1500 s after the release, we observe that the carbon dioxide is almost

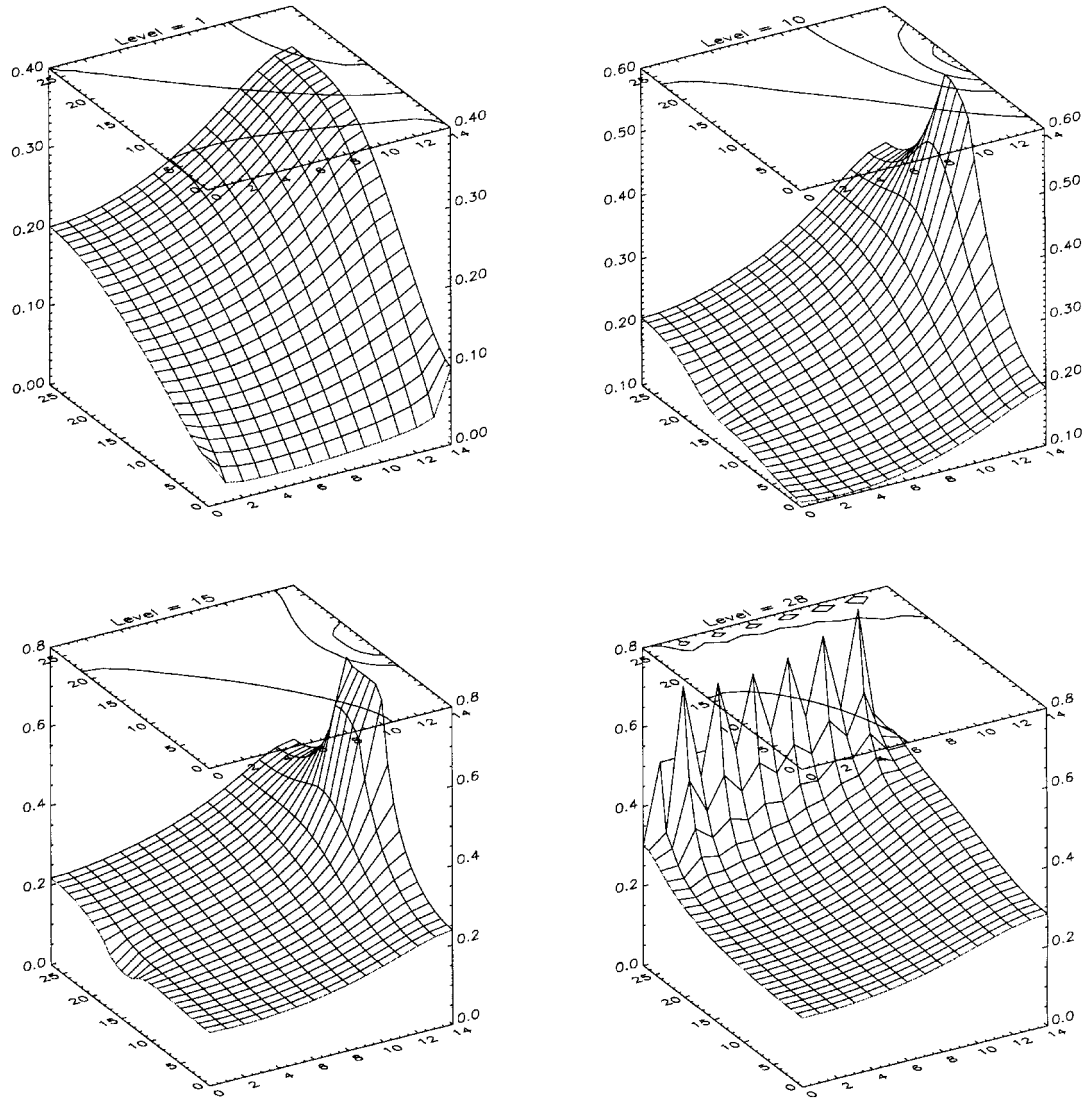

Fig. 8 Steady-state contamination profiles for the cabin.

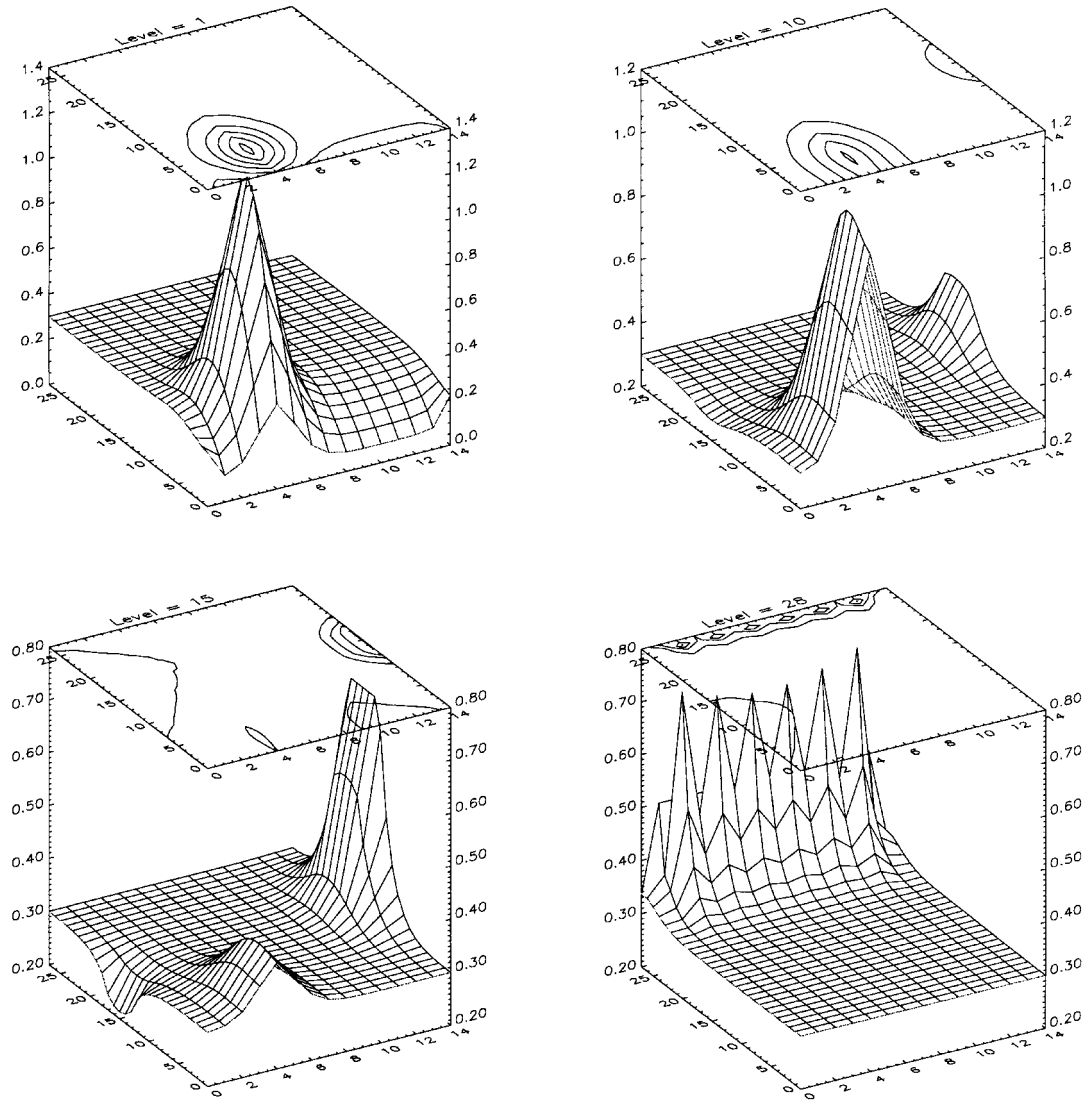

Fig. 9 Contamination profiles 90 s after a sudden carbon dioxide release.

well mixed, with only a slight bulge at the location of the release in the top slice. By this time, it is the flow profile that largely decides the contamination concentration profile.

Note here that there is a significant variation in the concentrations across the room, which might mean that lumped models of the cabin would be grossly inaccurate. Also, there are regions of accumulation in the room. This could mean that SMAC could be locally violated, even though the concentration averaged over the entire cabin may be below the SMAC limit. The flowfield is an important parameter in the way contaminants spread through the cabin and needs to be closely monitored.

State Estimation of Contaminant Concentration

The state estimation procedure closely follows that proposed by Skliar and Ramirez.[14] Estimation is necessary because there are always uncertainties, e.g., faults in the system, errors in the model, and changes in parameters that can cause real concentrations to be different from those predicted by the model. The objective of the filtering process is to arrive at an estimate that is unbiased, i.e., that has the smallest error in the least-square sense, and that gives an accurate picture of the actual system. The cost of sensors is high, which gives rise to the issues of placement and number of sensors. The estimation process is very crucial to the fault detection and diagnosis process because the matrices and calculations used in this procedure are used to make inferences about whether and where a fault (contaminant leak) has occurred.

The estimation problem, formulated simply, is as follows. Given a stochastic process that represents a dynamic system, we are interested in knowing the value of $\boldsymbol{x}(k)$ for some fixed k, where $\boldsymbol{x}(k)$ is not directly accessible to us for observation. We have a sequence of measurements that are causally related to $\boldsymbol{x}(k)$ by means of a measurement system M, and we wish to utilize these data to infer the value of $\boldsymbol{x}(k)$. We denote the estimate of $\boldsymbol{x}(k)$ by $\hat{\boldsymbol{x}}(k)$ and define it to be some n-dimensional, vector valued function $\boldsymbol{\Phi}_k$ of the measurements, viz.,

$$\hat{\boldsymbol{x}}(k \mid j) = \boldsymbol{\Phi}_k[z(i), i = 1, \ldots, j] \tag{10}$$

Crucial to the estimation process is the definition and notion of the estimation error, which is defined by the relation

$$\tilde{\boldsymbol{x}}(k \mid j) = \boldsymbol{x}(k) - \hat{\boldsymbol{x}}(k \mid j) \tag{11}$$

Ideally, $\tilde{\boldsymbol{x}} = 0$ and the estimate is exact. When this is not the case, we assign a penalty for the incorrect estimate. This is done through a penalty or a loss function l, which has the following properties.[15]

1) The loss function is a scalar-valued function of n variables.

2) Loss function $l(0) = 0$. There is no penalty if the estimate is exact.

3) Loss function l is a nondecreasing function of the distance of the error from the origin in n-dimensional Euclidean space.

4) Loss function l is symmetric about the origin.

One of the classical methods of state estimation is the well-established Kalman filtering algorithm. In the Kalman filtering paradigm, the uncertainties of the model and the measurements are represented by additive stochastic white noise.

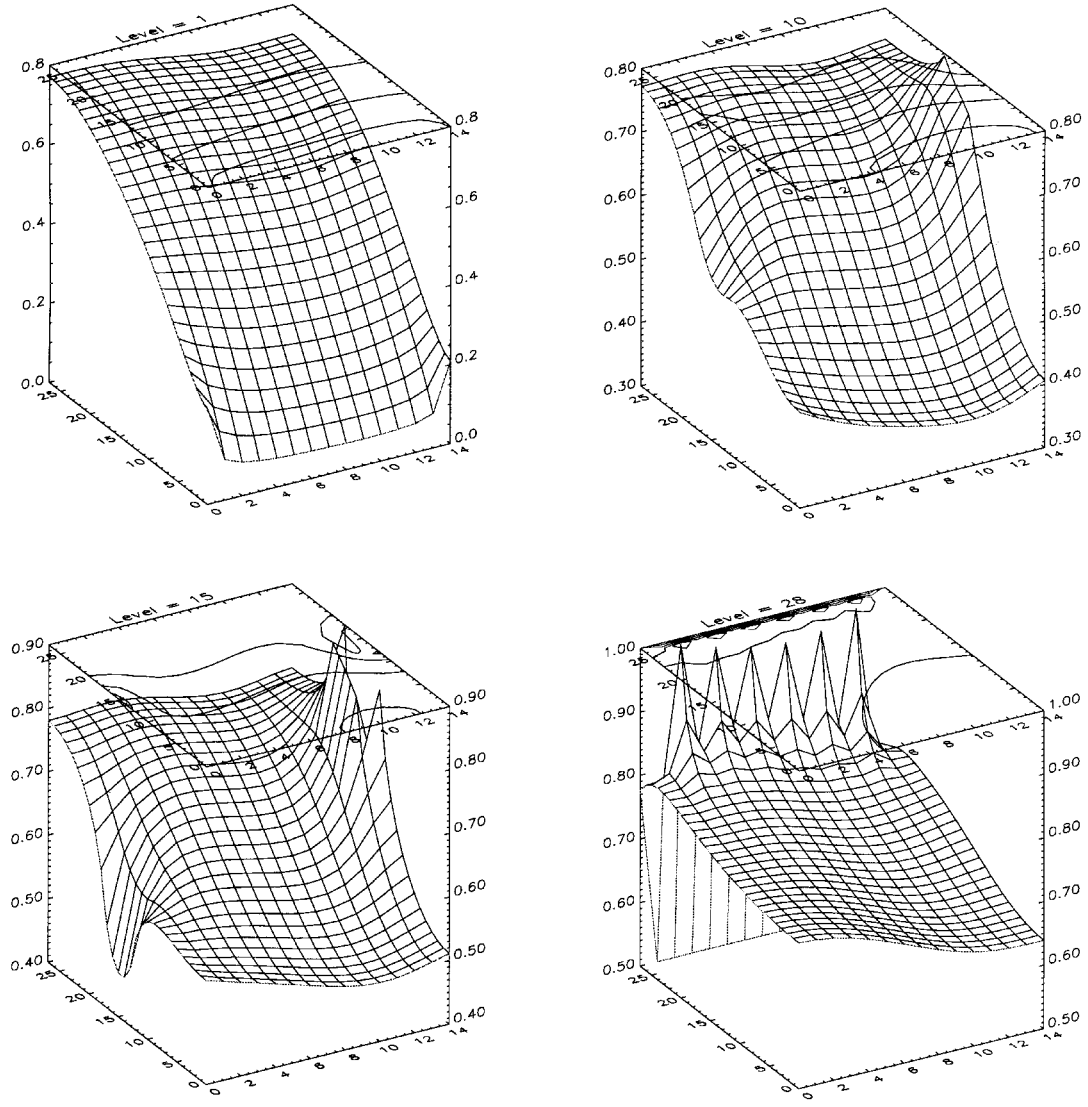

Fig. 10 Contamination profiles about 1500 s after the sudden release of carbon dioxide.

If we recast the model equations and include the additive noise, the model can be written as a single matrix equation

$$\boldsymbol{A}_1\boldsymbol{Q}_{m+1} = \boldsymbol{A}_2\boldsymbol{Q}_m + \begin{bmatrix} \boldsymbol{f}_m \\ \boldsymbol{0} \\ \boldsymbol{0} \end{bmatrix} + \begin{bmatrix} \boldsymbol{C}(m) \\ \boldsymbol{0} \\ \boldsymbol{0} \end{bmatrix} \boldsymbol{\alpha}_m \tag{12}$$

where

$$\boldsymbol{Q}_m = \begin{bmatrix} \boldsymbol{q}_m^* \\ \boldsymbol{q}_m^{**} \\ \boldsymbol{q}_m \end{bmatrix} \tag{13}$$

$$\boldsymbol{A}_1 = \left\{\boldsymbol{A}_1^{ij}\right\} = \begin{bmatrix} \left(\dfrac{-\boldsymbol{A}_x}{2} - \dfrac{\boldsymbol{r}}{\Delta t}\right) & \boldsymbol{0} & \boldsymbol{0} \\ \dfrac{\boldsymbol{r}}{\Delta t} & \left(\dfrac{-\boldsymbol{A}_y}{2} - \dfrac{\boldsymbol{r}}{\Delta t}\right) & \boldsymbol{0} \\ \boldsymbol{0} & \dfrac{\boldsymbol{r}}{\Delta t} & \left(\dfrac{-\boldsymbol{A}_z}{2} - \dfrac{\boldsymbol{r}}{\Delta t}\right) \end{bmatrix} \tag{14}$$

and

$$\boldsymbol{A}_2 = \boldsymbol{A}_2^{ij} = \begin{bmatrix} \boldsymbol{0} & \boldsymbol{0} & (\boldsymbol{A}_x/2 + \boldsymbol{A}_y + \boldsymbol{A}_z - \boldsymbol{r}/\Delta t) \\ \boldsymbol{0} & \boldsymbol{0} & -\boldsymbol{A}_y/2 \\ \boldsymbol{0} & \boldsymbol{0} & -\boldsymbol{A}_z/2 \end{bmatrix} \tag{15}$$

and

$$\boldsymbol{z}_{m+1} = [\boldsymbol{0} \quad \boldsymbol{0} \quad \boldsymbol{H}(m+1)]\,\boldsymbol{Q}_{m+1} + \boldsymbol{\beta}_{m+1} \tag{16}$$

The estimation of the contaminant concentration is determined from the sequential solution to the following tridiagonal equations:

$$\begin{aligned} &(-\boldsymbol{A}_x/2 - \boldsymbol{r}/\Delta t)\boldsymbol{q}^* = (\boldsymbol{A}_x/2 + \boldsymbol{A}_y + \boldsymbol{A}_z - \boldsymbol{r}/\Delta t)\boldsymbol{q}_m \\ &\quad + \boldsymbol{f}_m + \boldsymbol{L}_1[\boldsymbol{z} - \boldsymbol{H}_1\hat{\boldsymbol{y}}_{m+1|m}] \\ &(-\boldsymbol{A}_y/2 - \boldsymbol{r}/\Delta t)\boldsymbol{q}^{**} = -(\boldsymbol{A}_y/2)\boldsymbol{q}_m - (\boldsymbol{r}/\Delta t)\boldsymbol{q}^* \\ &\quad + \boldsymbol{L}_2[\boldsymbol{z} - \boldsymbol{H}_1\hat{\boldsymbol{y}}_{m+1|m}] \\ &(-\boldsymbol{A}_z/2 - \boldsymbol{r}/\Delta t)\boldsymbol{q}_{m+1} = -(\boldsymbol{A}_z/2)\boldsymbol{q}_m - (\boldsymbol{r}/\Delta t)\boldsymbol{q}^{**} \\ &\quad + \boldsymbol{L}_3[\boldsymbol{z} - \boldsymbol{H}_1\hat{\boldsymbol{y}}_{m+1|m}] \end{aligned} \tag{17}$$

where the predicted estimation of the auxiliary variable $\boldsymbol{y} = \boldsymbol{A}_1\boldsymbol{Q}$ is given by the following equation:

$$\hat{\boldsymbol{y}}_{m+1|m} = \begin{bmatrix} \boldsymbol{A}_2^{13} \\ \boldsymbol{A}_2^{23} \\ \boldsymbol{A}_2^{33} \end{bmatrix} \hat{\boldsymbol{q}}_{m|m} + \begin{bmatrix} \boldsymbol{f}_m \\ \boldsymbol{0} \\ \boldsymbol{0} \end{bmatrix} \tag{18}$$

The modified measurement matrix $\boldsymbol{H}_1 = \boldsymbol{H}_{1j}$ is calculated using the following equation:

$$[\boldsymbol{H}_{11} \quad \boldsymbol{H}_{12} \quad \boldsymbol{H}_{13}]\boldsymbol{A}_1 = [\boldsymbol{0} \quad \boldsymbol{0} \quad \boldsymbol{H}] \tag{19}$$

which is equivalent to solving the following equations:

$$\boldsymbol{H}_{13}\boldsymbol{A}_1^{33} = \boldsymbol{H}, \qquad \boldsymbol{H}_{12}\boldsymbol{A}_1^{22} = -\boldsymbol{H}_{13}\boldsymbol{A}_1^{32}, \qquad \boldsymbol{H}_{11}\boldsymbol{A}_1^{11} = -\boldsymbol{H}_{12}\boldsymbol{A}_1^{21} \tag{20}$$

The implicit Kalman gain is given by the equation

$$\boldsymbol{L}_{m+1} = \boldsymbol{P}^y_{m+1|m}\boldsymbol{H}_1^T\left[\boldsymbol{H}_1\boldsymbol{P}^y_{m+1|m}\boldsymbol{H}_1^T + \boldsymbol{R}(m+1)\right]^{-1} \tag{21}$$

where

$$\boldsymbol{P}^y_{m+1|m} = \begin{bmatrix} \boldsymbol{A}_2^{13}\boldsymbol{P}^q_{m|m}\boldsymbol{A}_2^{13^T} + \boldsymbol{CQC}^T & \boldsymbol{A}_2^{13}\boldsymbol{P}^q_{m|m}\boldsymbol{A}_2^{23^T} & \boldsymbol{A}_2^{13}\boldsymbol{P}^q_{m|m}\boldsymbol{A}_2^{33^T} \\ \boldsymbol{A}_2^{23}\boldsymbol{P}^q_{m|m}\boldsymbol{A}_2^{13^T} & \boldsymbol{A}_2^{23}\boldsymbol{P}^q_{m|m}\boldsymbol{A}_2^{23^T} & \boldsymbol{A}_2^{23}\boldsymbol{P}^q_{m|m}\boldsymbol{A}_2^{33^T} \\ \boldsymbol{A}_2^{33}\boldsymbol{P}^q_{m|m}\boldsymbol{A}_2^{13^T} & \boldsymbol{A}_2^{33}\boldsymbol{P}^q_{m|m}\boldsymbol{A}_2^{23^T} & \boldsymbol{A}_2^{33}\boldsymbol{P}^q_{m|m}\boldsymbol{A}_2^{33^T} \end{bmatrix} \tag{22}$$

$$\boldsymbol{P}^y_{m+1|m+1} = [\boldsymbol{I} - \boldsymbol{L}_{m+1}\boldsymbol{H}_1]\boldsymbol{P}^y_{m+1|m} \tag{23}$$

and

$$\boldsymbol{P}^y_{m+1|m+1} = \boldsymbol{A}_1\boldsymbol{P}^Q_{m+1|m+1}\boldsymbol{A}_1^T \tag{24}$$

Note that the main filter Eq. (17) is identical in structure to the model equation in Eq. (12), the only difference being the addition of the last term, which is the effect of the filter on the equations.

The solution to the last equation is reduced to a sequential solution of the following six tridiagonal equations:

$$\boldsymbol{A}_1^{11}\left[\boldsymbol{P}^Q_{m+1|m+1}\right]^{11}\boldsymbol{A}_1^{11^T} = \left[\boldsymbol{P}^y_{m+1|m+1}\right]^{11}$$

$$\boldsymbol{A}_1^{11}\left[\boldsymbol{P}^Q_{m+1|m+1}\right]^{12}\boldsymbol{A}_1^{22^T} = \left[\boldsymbol{P}^y_{m+1|m+1}\right]^{12} - \boldsymbol{A}_1^{11}\left[\boldsymbol{P}^Q_{m+1|m+1}\right]^{11}\boldsymbol{A}_1^{21^T}$$

$$\boldsymbol{A}_1^{11}\left[\boldsymbol{P}^Q_{m+1|m+1}\right]^{13}\boldsymbol{A}_1^{33^T} = \left[\boldsymbol{P}^y_{m+1|m+1}\right]^{13} - \boldsymbol{A}_1^{11}\left[\boldsymbol{P}^Q_{m+1|m+1}\right]^{12}\boldsymbol{A}_1^{32^T}$$

$$\boldsymbol{A}_1^{22}\left[\boldsymbol{P}^Q_{m+1|m+1}\right]^{22}\boldsymbol{A}_1^{22^T} = \left[\boldsymbol{P}^y_{m+1|m+1}\right]^{22} - \boldsymbol{A}_1^{21}\left[\boldsymbol{P}^Q_{m+1|m+1}\right]^{11}\boldsymbol{A}_1^{21^T} - \boldsymbol{A}_1^{21}\left[\boldsymbol{P}^Q_{m+1|m+1}\right]^{12}\boldsymbol{A}_1^{22^T} - \left[\boldsymbol{A}_1^{21}\left[\boldsymbol{P}^Q_{m+1|m+1}\right]^{12}\boldsymbol{A}_1^{22^T}\right]^T$$

$$\boldsymbol{A}_1^{22}\left[\boldsymbol{P}^Q_{m+1|m+1}\right]^{23}\boldsymbol{A}_1^{33^T} = \left[\boldsymbol{P}^y_{m+1|m+1}\right]^{23} - \boldsymbol{A}_1^{21}\left[\boldsymbol{P}^Q_{m+1|m+1}\right]^{12}\boldsymbol{A}_1^{32^T} - \boldsymbol{A}_1^{22}\left[\boldsymbol{P}^Q_{m+1|m+1}\right]^{22}\boldsymbol{A}_1^{32^T} - \boldsymbol{A}_1^{21}\left[\boldsymbol{P}^Q_{m+1|m+1}\right]^{13}\boldsymbol{A}_1^{33^T}$$

$$\boldsymbol{A}_1^{33}\left[\boldsymbol{P}^Q_{m+1|m+1}\right]^{33}\boldsymbol{A}_1^{33^T} = \left[\boldsymbol{P}^y_{m+1|m+1}\right]^{33} - \boldsymbol{A}_1^{32}\left[\boldsymbol{P}^Q_{m+1|m+1}\right]^{22}\boldsymbol{A}_1^{32^T} - \boldsymbol{A}_1^{32}\left[\boldsymbol{P}^Q_{m+1|m+1}\right]^{23}\boldsymbol{A}_1^{33^T} - \left[\boldsymbol{A}_1^{32}\left[\boldsymbol{P}^Q_{m+1|m+1}\right]^{23}\boldsymbol{A}_1^{33^T}\right]^T \tag{25}$$

where

$$\left[\boldsymbol{P}^Q_{m+1|m+1}\right]^{33} = \boldsymbol{P}^q_{m+1|m+1}$$

We can now formulate the algorithm of the estimation of the contaminant concentration $\boldsymbol{q}_{m+1}$ based on the measurement data and the transport model.

1) Compute $\hat{\boldsymbol{y}}_{m+1|m}$ by propagating $\hat{\boldsymbol{q}}_{m|m}$ according to Eq. (18).

2) Successively solve three tridiagonal matrix equations for the modified measurement matrix $\boldsymbol{H}_1$.

3) Solve the tridiagonal model equations with the new perturbation to obtain the optimal estimate $\boldsymbol{q}_{m+1|m+1}$.

The calculation of the gain $\boldsymbol{L}_{m+1}$ of the implicit Kalman filter follows the following algorithm.

1) Calculate $\boldsymbol{P}^y_{m+1|m}$ according to Eq. (22).

2) Calculate the implicit Kalman filter gain using Eq. (21).

3) Calculate $\boldsymbol{P}^y_{m+1|m+1}$ according to Eq. (23).

4) The final step is to initiate the gain calculation for the next time step, for which one sequentially solves Eq. (25). This is by far the most time-consuming step.

Filter Implementation and Testing

A true test of the filter can occur only in an experimental setting with a physical cabin and measurements. In the absence of that, we tested the filter using the results of the model itself. We added a random Gaussian noise to the contaminant concentrations from the model, as we would expect to get in a real setting, and then checked to see whether the filter was able to track the contaminant concentrations to sufficient accuracy.

The filter is a computationally intensive program, and we found that it was taking around 30 s for each time step on a DEC-Alpha Station 250 4/266. Therefore, we ran the model and the filter with a 30-s time step. We are using a set of five sensors to estimate the concentration in the whole room. Table 1 shows the location of each of the sensors, which are distributed throughout the cabin. The cabin is represented by a mesh that is 14 × 28 × 30, and the sensor positions are given in terms of the mesh coordinates.

Table 1 Sensor location and the associated measurement and model noise

Sensor	Coordinates	Q_{diag}	R_{diag}
1	10, 10, 10	0.0001	0.0001
2	8, 2, 23	0.0001	0.0001
3	3, 5, 7	0.0001	0.0001
4	6, 6, 6	0.0001	0.0023
5	4, 11, 22	0.0001	0.00019
6	8, 14, 18	0.0001	0.00019

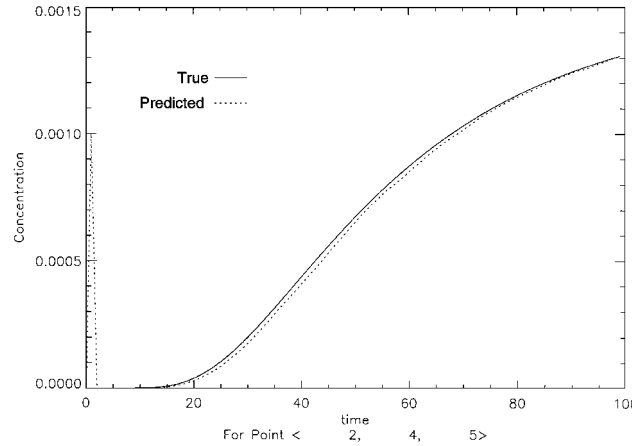

Fig. 11 Filter performance; tracking concentrations at an arbitrary point in the lower-left-hand portion of the cabin.

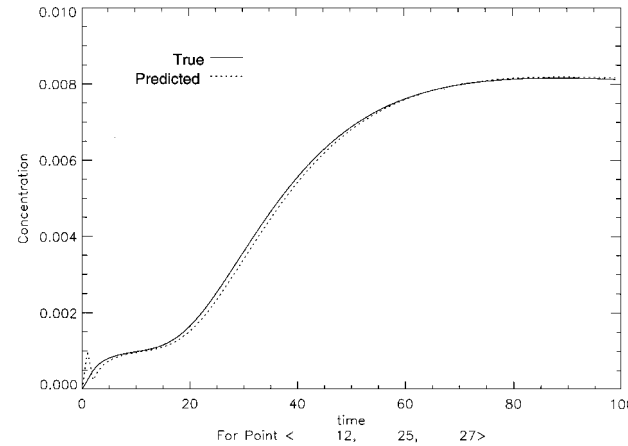

Fig. 12 Filter performance; tracking concentrations at an arbitrary point in the upper-right-hand portion of the cabin.

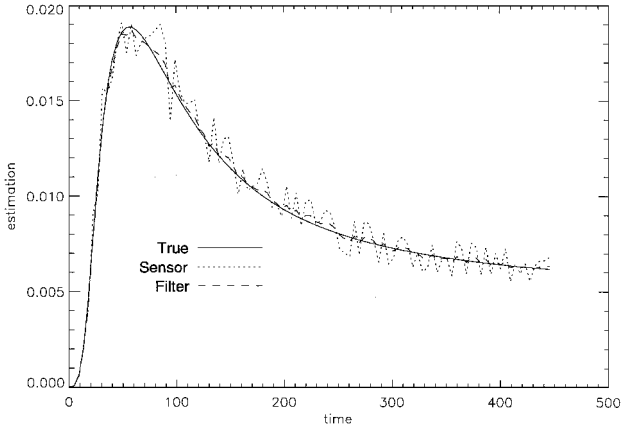

Fig. 13 Filter performance; tracking at sensor location 1.

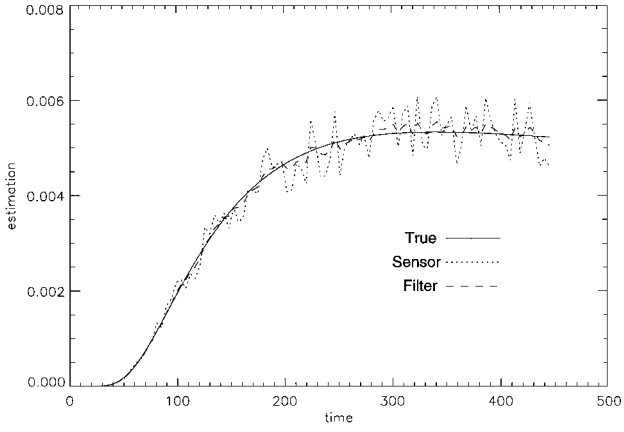

Fig. 14 Filter performance; tracking at sensor location 2.

The graphs show the results of the contaminant concentration estimation for 30 time steps. Figures 11 and 12 show the tracking of the concentrations at two arbitrary points in the domain, and Figs. 13 and 14 show how the filter performs at the sensor locations in the presence of measurement noise. The filter serves to filter out the measurement noise while still reconciling the model and the sensor readings, which can be observed from the figures. The tracking is fairly accurate and is mathematically consistent.

The results from the filter serve as an input to the alarm system, the discussion of which is beyond the scope of this paper. The residual error between the model prediction and the measurements is used for this purpose, and when it exceeds a certain threshold level, an alarm is raised.

Conclusions

We have developed and discussed the design and implementation of an accurate and intelligent contaminant monitoring system for the space station. The use of advanced CFD techniques in tracking the airflow greatly increases the accuracy of the results. We use a three-dimensional implicit Kalman filter for the state prediction and discuss the tracking performance in the presence of uncertainty. We found that a time step of about 30 s results in real-time performance of the tracking system, given our current computational power. Further mathematical development should give rise to an efficient and accurate real-time tracking system for contaminants and match the advanced technology requirements of a tracking time interval of 15 s.

Acknowledgments

This work was partially supported by NASA under NAGW-4585 and utilized the Silicon Graphics Power Challenge Array at the National Center for Supercomputing Applications, University of Illinois at Urbana–Champaign. We wish to thank our anonymous reviewers for their comments and suggestions.

References

[1] Skliar, M., "State Estimation and Fault Diagnosis for Distributed Parameter Transport Processes with Application to Air Contamination Control," Ph.D. Thesis, Dept. of Chemical Engineering, Univ. of Colorado, Boulder, CO, 1996.

[2] Perry, J. L., "Computerized Atmospheric Trace Contaminant Simulation for Manned Spacecraft," NASA TM-108409, June 1993.

[3] Skliar, M., and Ramirez, W. F., "Air-Quality Monitoring and Detection of Air Contamination in an Enclosed Environment," *Journal of Spacecraft and Rockets,* Vol. 34, No. 4, 1997, pp. 522–532.

[4] Douglas, J., Jr., and Rachford, H. H., Jr., "On the Numerical Solution of Heat Conduction Problems in Two and Three Space Variables," *Transactions of the American Mathematical Society*, Vol. 82, July 1956, pp. 421–439.

[5] Godunov, S. K., "Finite Difference Method for Numerical Computation of Discontinuous Solutions of the Equations of Fluid Dynamics," *Matematicheskii Sbornik*, Vol. 47, No. 3, 1959, pp. 271–306.

[6] Kurabuchi, T., Fang, J. B., and Grot, R. A., "A Numerical Method for Calculating Indoor Airflows Using a Turbulence Model," National Inst. of Standards and Technology, NISTIR 89-4211, Gaithersburg, MD, Jan. 1990.

[7] Whittle, G. E., and Clancy, E. M., "Evaluation of Cases B, D, E—Presentation of Results from Measurements and Simulations," International Energy Agency Annex 20 Research Rept., Swedish Council for Building Research, D0283-8761, Nov. 1991.

[8] Barber, E. M., Sokgansanj, S., Lapman, W. P., and Ogilvie, J. R., "Stability of Air Flow Patterns in Ventilated Spaces," American Association of Agricultural Engineers, Paper 82-4551, 1982.

[9] Neilsen, P. V., "Air Distribution System—Room Air Movement and Ventilation Effectiveness," *Room Air Convection and Ventilation Effectiveness*, American Society of Heating, Refrigeration and Air-Conditioning Engineers, Inc., Atlanta, GA, 1992, pp. 43–52.

[10] Zhang, J. S., Wu, G. J., and Christianson, L. L., "Full-Scale Experimental Results on the Mean and Turbulent Behavior of Room Ventilation Flows," *ASHRAE Transactions*, Vol. 98, No. 2, 1992, pp. 307–318.

[11] Son, C., and Barker, R. S., "U.S. Lab—A Module Cabin Air Distribution in Space Station," Society of Automotive Engineers, SAE 932192, Warrendale, PA, July 1993.

[12] "FIDAP Users Manual," Revision 7.0, Fluid Dynamics International, Inc., Evanston, IL, April 1993.

[13] Anderson, D. A., Tannenhill, J. C., and Pletcher, R. H., *Computational Fluid Mechanics and Heat Transfer*, McGraw–Hill, New York, 1984, pp. 221–235.

[14] Skliar, M., and Ramirez, W. F., "Implicit Kalman Filtering," *International Journal of Control*, Vol. 66, No. 3, 1997, pp. 393–412.

[15] Meditch, J. S., *Stochastic Optimal Linear Estimation and Control*, McGraw–Hill, New York, 1969, pp. 159–175.

I. D. Boyd
Associate Editor